STARS

Electronic Theses and Dissertations, 2020-

2020

High-Speed Interferometry and Visible Videography for Meniscus Curvature Analysis during Anisotropic Hemiwicking

John Bal

University of Central Florida

Part of the Mechanical Engineering Commons

Find similar works at: https://stars.library.ucf.edu/etd2020

University of Central Florida Libraries http://library.ucf.edu

STARS Citation

Bal, John, "High-Speed Interferometry and Visible Videography for Meniscus Curvature Analysis during Anisotropic Hemiwicking" (2020). *Electronic Theses and Dissertations, 2020-*. 11.
https://stars.library.ucf.edu/etd2020/11

HIGH-SPEED INTERFEROMETRY AND VISIBLE VIDEOGRAPHY FOR MENISCUS
CURVATURE ANALYSIS DURING ANISOTROPIC HEMIWICKING

by

JOHN RYAN BAL
B.S. University of Central Florida, 2019

A thesis submitted in partial fulfillment of the requirements
for the degree of Master of Science
in the Department of Mechanical and Aerospace Engineering
in the College of Engineering and Computer Science
at the University of Central Florida
Orlando, Florida

Spring Term
2020

ABSTRACT

Recent advancements in microelectronics have increased the need for thermal management systems capable of high heat flux dissipation within significant spatial constraints. One method of increasing local heat fluxes is the fabrication of superhydrophilic materials via micro/nanostructuring of the surface.   Superhydrophilic surfaces act in a self-pumping capacity, spreading fluid beyond its intrinsic meniscus length to form thin-films, a process known as "hemiwicking", with practical applications in evaporative cooling, as well as flow, pool, and thin-film boiling. Of particular interest is anisotropic hemiwicking via asymmetric microstructuring. The microscopic asymmetricity of the design induces a macroscopically preferred direction of wicking, which has the potential to be tailored to specific heating configurations for increased efficiencies. In this study, half-conical asymmetric microstructures have been produced via two-photon polymerization, and anisotropic quality has been characterized through the use of high-speed videography. High-speed thin-film interferometry and microscopic side-angle videography are utilized to study the evolution of meniscus curvature during inter-pillar fluid front propagation, which determines driving force via Laplace pressures. Experimental results show increased meniscus curvature in the preferred direction of wicking, and measurements at later time scales are in agreement with traditional curvature scaling laws. Meniscus stability differences are also observed during initial front propagation. These results can be used to help optimize anisotropic hemiwicking designs for use in next-generation heat sinks.

ACKNOWLEDGMENTS

I would first like to express my complete and utter appreciation for my advisor, Dr. Shawn A. Putnam. I met Dr. Putnam as a sophomore taking an honors thermodynamics course, and he has been an incredible mentor and advisor to me ever since. He convinced me to pursue an accelerated B.S. to M.S. track early on, without which I would not be in the place I am today. His willingness to push his students has led, not only to my personal development as an engineer, but to the development of every member of our laboratory group from a student to a professional ready to take on the world. He has challenged us to think outside the box and to approach any and all intellectual challenges with an open mind. For his mentorship I am extremely grateful.

I would like to thank the National Science Foundation for partially sponsoring the work that has been completed and is enclosed in this thesis. Without proper funding, none of this would have been possible.

Fabrication of microstructured surfaces was conducted at the Center for Nanophase Materials Sciences, which is a DOE Office of Science User Facility. To Oak Ridge National Laboratory Center for Nanophase Material Science Nanofabrication Lab, I extend my heartfelt gratitude. While I could in no way mention every member that helped along the way towards fabrication of these samples, there are a number of specific individuals that went out of their way to assist me before, during, and after my visit to ensure the process was completed properly. First and foremost, Dr. Bernadeta Srijanto, my main contact at ORNL, communicated with me for months leading up to the fabrication of samples, fabricated test samples prior to my arrival, and stayed past hours during my visit to ensure the entire process ran smoothly. I would also like to

iii

TABLE OF CONTENTS

LIST OF FIGURES

LIST OF TABLES

CHAPTER 1: INTRODUCTION

<u>Background</u>

Due to constantly evolving spatial constraints and increasing heat flux requirements, microelectronic heat-mitigating technologies have recently begun to focus on improvements in applicable microscale heat transfer techniques. Traditional methods, such as forced air convection over solid heat sinks, simply do not have the capacity to effectively manage the increasingly large heat fluxes that are being produced in single microelectromechanical systems (MEMS). These new microscale techniques, including jet-impingement, spray cooling, and microchannel cooling, offer vastly improved heat flux performances for small surface areas compared to traditional methods [1], [2].

Wall dry-out is a phenomenon in boiling where bubble nucleation occurs so rapidly that an insulatory vapor layer forms over the solid surface and prevents rewetting of the surface. This results in a localized temperature spike as the resistance across the thermal network drastically increases. The temperature spike results in a further increase in the insulatory vapor layer, further increasing the temperature. This viscous cycle quickly results in wall dry-out, also termed "burn out" and "thermal runaway", and failure of the cooling system. In order to operate systems at increasingly necessary higher temperatures (and therefore higher heat fluxes), delaying the formation of this insulatory vapor layer is imperative.

New focuses on physically microstructured and chemically patterned surfaces have emerged for delaying wall dry-out in critical heat flux conditions, as well as maintaining a steady meniscus for thin-film evaporation [3], [4]. This makes these engineered surfaces applicable for

both high-temperature and low-temperature requirements. These microstructured surfaces can act in a self-pumping capacity, utilizing capillary forces to propel a fluid beyond its intrinsic meniscus extension, creating a superhydrophilic surface [5]. Such fluid motion, occurring in the Stoke's flow regime, is termed "hemiwicking". These superhydrophilic surfaces result in increased Critical Heat Flux (CHF) conditions by increasing the wettability of a surface, and therefore delaying the formation of the insulatory vapor layer [3].

Various studies have been published detailing the diffusive nature of the hemiwicking process [6], [7], [8], [9]. These studies often derive the forcing function (also known as driving function) of a hemiwicking process via macroscale surface energy minimization or pressure differentials caused by a curved liquid meniscus.

Anisotropic wetting is a phenomena caused by asymmetric microstructuring of a surface. Asymmetric microstructures have come into focus as an especially effective method of tailoring a cooling system to pump fluids through specific heating configurations by utilizing complex flow patterns. The ability to control the mass flux of cooling fluid in various directions through a microchannel or over a microstructured heat sink could enable more effective localized cooling in these conditions. Understanding the complicated intermolecular and interfacial interactions that accompany an anisotropic hemiwicking flow is necessary for predicting and optimizing the performance of these structured implemented in self-regulating cooling technologies.

Many experiments have been performed on asymmetrically structured surfaces that exhibit either anisotropic wetting conditions in perpendicular directions, or anisotropic to unidirectional hemiwicking motions [10], [11], [12], [13], [14]. Xia et al. investigated anisotropic wetting via

2

the use of surface ridges in lieu of microstructures [11]. They were able to exhibit anisotropic droplet wetting in perpendicular directions via the use of these ridges, which formed physical barriers for liquid propagation perpendicular to the ridges. Jokenin et al. utilized triangular microstructures to achieve parallel anisotropic wetting (wetting of differing velocities in opposite directions) as well as unidirectional wetting [14]. The stability of the meniscus formation was found to be the main cause of asymmetry in the microstructures. The formation of uneven menisci curvatures leading to Laplace pressure differences has been noted in asymmetric microstructures implemented along open micro-channels [13].

<p align="center">Research Focus and Motivation</p>

It has been stated the clear application of superhydrophilic microstructured surfaces for enhanced cooling via flow boiling, pool boiling, thin-film boiling, and thin-film evaporation. Increasing the temperature at which dry-out occurs would allow for MEMS operation at higher temperatures, and therefore high heat fluxes.

The cause of anisotropy in wetting is, by its very nature, a microscopic process. Application of hemiwicking models that utilize macroscale surface energy minimization to asymmetric microstructures will inherently cause deviations. It is important that the microscale dynamics of asymmetric meniscus formation and curvature are implemented into models to account for anisotropic wetting characteristics, however, a full model is yet to be realized in the literature.

Half-conical asymmetric micropillar surfaces were fabricated, and anisotropic wetting characteristics were observed during hemiwicking propagation; fluid propagation rates varied depending on the alignment of the microstructures with the flow direction. Experiments were

performed in order to classify the level of anisotropy via macroscale propagation, as well as to study the source of anisotropic wetting behavior caused by surface roughness asymmetry at a microscopic level. Via the use of both side-angle videography and high-speed interferometry, it is possible to investigate both the stability of the climbing meniscus and film curvature development within the propagating front of the fluid film, as the fluid propagates in both the preferred and non-preferred directions. The half-conical design of the micropillars themselves should lead to variations in both meniscus stability and curvature as the flow propagates between two pillars.

CHAPTER 2: LITERATURE REVIEW

Stokes Flow Dynamics

In order to fully comprehend the phenomena described in this thesis, a brief review of Stokes flow dynamics must be undertaken. Stokes flow has been described as a flow in which the inertia of a fluid can be ignored when compared to viscous effects [15]. The upper limit of this regime has historically been classified by the Reynold's number being on the order of unity ($Re \leq 1$) [16]. Consequently, these flows will generally occur either with an extremely low velocity (for this reason, another term for Stoke's flow is "creeping flow") or around objects with an extremely small characteristic length. When inertial terms can be neglected, it is common to solve the system by summing forces and setting equal to zero. As a result, in later sections, driving forces are often balanced by resistive (drag) forces in order to analytically solve the system.

Few exact solutions for the flow field (and therefore drag) around objects in the Stokes flow region have been solved. Those that have been solved often involve simple shapes such as spheres, ellipsiods, and elongated rods [15]. General solutions for the flow field far from the body in question have been studied extensively, but solutions directly adjacent to the body are needed in order to predict the drag around such bodies. The primary Green's functions for solving flow around more complicated bodies are the Stokeslets, rotlets, and doubletand stresslets, which represent spatial distributions of singular forces, torques, and other flow singularities [15].

Wetting

The complicated study of wetting dynamics has received increased attention over the years due to its use in a number of practical engineering applications [17]. Below, a review of some of

5

the most important equations in wetting dynamics is presented, along with recent development in modifying surface parameters in order to induce changes in wetting properties.

Young-Dupre Equation

The famous Young-Dupre Equation relates the solid-vapor, solid-liquid, and liquid-vapor surface tensions in the thermodynamic equilibrium case to the contact angle. It is given by:

$$\gamma_{LV} \cos(\theta) = \gamma_{SV} - \gamma_{SL} \tag{1}$$

where γ is the surface tension (dimensions energy/area or force/length), and θ is the equilibrium contact angle [18]. The regimes of wetting are defined from Eq. 1. For an equilibrium contact angle less than 90°, $\gamma_{SV} < \gamma_{SL}$, which implies from energy minimization that a non-wetted surface is preferred. The opposite case applies: for an equilibrium contact angle greater than 90°, $\gamma_{SV} > \gamma_{SL}$ and a wetted surface is preferred. The "wettability" of a surface is therefore often characterized by the equilibrium contact angle [19].
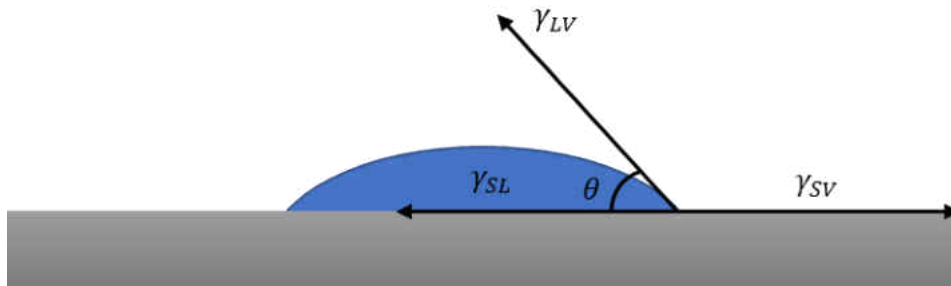
Figure 1: Equilibrium contact angle and surface tension forces describing the Young-Dupre Equation (Eq. 1).

This equation has, in the past, been used to explain the work of adhesion for a liquid droplet on a solid surface, given by Adam and Livingston in Eq. 2 [20].

$$W_A = \gamma_{LV}[1 + \cos(\theta)] \tag{2}$$

Modifying Wetting Properties

It can be seen from Eq. 1 that varying both surface energy and fluid properties will influence the wettability of the system. The two main methods for varying the surface energy of a system are through introducing chemical heterogeneities and surface roughness elements. Below, the defining equations for these variations are presented, and explanations on current research topics based on these methods are detailed.

Chemical Heterogeneities

Chemical heterogeneities are differences in surface energy properties across a solid surface. The length scale of such heterogeneities can be anywhere from nano-scale to macro-scale. The basis of all studies on chemical heterogeneities and wetting properties is the Cassie Equation, based on surface fraction of the various surfaces. In a multi-component solid with n components, the Cassie equation can be written in the form [21]:

$$\cos(\theta) = \sum_{k=1}^{n} \sigma_n \cos(\theta_n) \tag{3}$$

where σ_n and θ_n represent the surface fraction and equilibrium contact angle of the n'th component. However, many real-world experiments have failed to properly follow Eq. 3. One of the most pronounced issues that cannot be resolved by the Cassie Equation is that of wetting hysteresis [17]. While many authors have attempted to quantitatively account for wetting hysteresis in the advancing and receding cases, the main takeaway has been a qualitative one: "An advancing liquid will preferentially sample low-energy components, while a receding liquid will sample high-energy components, such that $\theta_a > \theta > \theta_r$ [17].

7

Priest et al. performed experiments utilizing the Wilhelmy plate technique in order to measure the effects of single chemically heterogeneous defects on wetting motion and study the added forces due to pinning of the liquid contact line during wetting and dewetting over the defect. They found that two cases occurred [17]:

1. The case of a high energy (with respect to the bulk solid) defect: advancing measurements deviated from theory while receding measurements agreed with theory.

2. The case of a low energy (with respect to the bulk solid) defect: receding measurements deviated from theory while advancing measurements agreed with theory.

Douglas Frink and Salinger studied the effects of non-local heterogeneities via a solid surface with alternating high-energy and low-energy strips [22]. They found that the contact angle depended on the size of the strips, which is in agreement with Eq. 3. The location of a wetting transition depended heavily on the size and strength of the chemical heterogeneity, and wetting hysteresis could be used to gauge the wetting transition across the heterogeneity.

Surface Roughness

Modifying surface roughness can have profound effects on the wetting behavior of a solid-liquid-vapor system. The first to quantitatively describe this phenomena was Wenzel, who showed that the equilibrium contact angle of a rough surface is related to the roughness and the equilibrium contact angle of the same liquid-vapor-solid system on a smooth surface [23]:

$$\cos(\theta^*) = r\cos(\theta) \tag{4}$$

where r, the roughness, is the ratio of the total surface area to the apparent surface area. It is apparent that $r \geq 1$.

It can be shown from this equation that introducing surface roughness will only amplify the wetting situation of the smooth surface; hydrophobic surfaces will become more hydrophobic and hydrophilic surfaces will become more hydrophilic, but a hydrophobic surface cannot become hydrophilic via surface roughening, and vice versa. Mathematically speaking, a hydrophilic surface ($\theta < 90°$) will have a positive cosine value that will only increase after roughening, resulting in a smaller contact angle, while a hydrophobic surface ($\theta > 90°$) will have a negative cosine value that will only increase in magnitude, resulting in a larger contact angle. The state of a droplet sitting on a rough surface that imbibes the roughness elements underneath it but does not extend beyond the bulk fluid is known as the Wenzel state, and the state in which a fluid will sit on-top of a roughness element without imbibing at all is known as the Cassie-Baxter state [24].

The concept of surface tension as an energy per unit area has persisted since the publishing of the original works of Cassie and Wenzel, but this viewpoint can lead to experimental results that clash with convention. For example, it has been found that a small patch of roughness under the bulk of a sessile droplet does not affect the equilibrium contact angles at all. It is, in fact, only the roughness at area of the contact line (length of contact line multiplied by some molecular distance) that effects the contact angle, so a better representation of the Wenzel equation could be given by [25]:

$$\cos(\theta^*(x, y)) = r(x, y)\cos(\theta) \tag{5}$$

This equation shows that roughness elements local to the contact line dominate the equilibrium dynamics of the system, rather than the roughness of the solid that's under a bulk fluid, or the average roughness of the system. It has been shown that Eq. 4 can similarly be modified to account for the local variations in surface energy [25]. Eq. 4 and 5 are still valid when the scale

9

of the surface roughness/heterogeneities are small compared to the length scale of the bulk fluid. It has also been shown that contact angle hysteresis is also a function of the contact line behavior rather than a function of the interfacial area [26].

<u>Hemiwicking</u>

According to Krishnan et al., "Hemiwicking is the phenomena where a liquid wets a textured surface beyond its intrinsic wetting length due to capillary action and imbibition" [6]. As opposed to the Wenzel state, where the fluid only imbibes the textured surface directly underneath the bulk liquid, the fluid during a hemiwicking motion will spread significantly beyond the bulk. This is achieved through systematic microstructuring with high roughness values [7]. The term hemiwicking denotes the process as an intermediate between liquid wetting and porous structure wicking [8]. Below, a brief review on capillary forces is presented, then a comparison of varying forcing functions and resisting functions in hemiwicking models is analyzed.
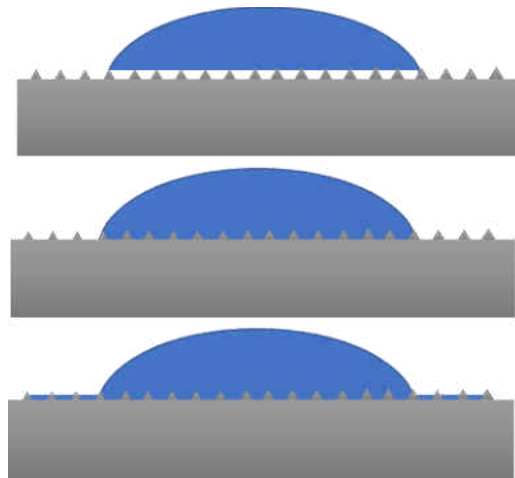
Figure 2: Diagram explaining the Cassie-Baxter state (top), Wenzel state (middle), and hemiwicking state (bottom).

Capillary Forces

Capillary forces drive many processes in both nature and industry [27]. It is a result of free energy minimization during a wetting process, forcing a fluid to wet a solid surface, flow through narrow channels against gravity, and wick through porous media [27], [28]. It is a function of the fluid's surface tension, solid-liquid contact angle, and length of contact line, given by:

$$f_{cap} = \gamma_{LV} L cos(\theta) \tag{6}$$

Capillary and viscous forces often dominate inertial forces in practical applications in microfluidics. Often, this is due to a small Reynold's number, but in other cases the application of the lubrication approximation gives the same result [27], [29]. Imbibition length into a capillary tube (L) with a circular cross section as a function of time is given by the famous Washburn equation:

$$L^2 = \frac{\gamma \cos(\theta)}{2\mu} Rt \tag{7}$$

where μ is the fluid's dynamic viscosity and r is the radius of the capillary tube [30]. Eq. 8 describes a diffusive process (in this case $D = \frac{\gamma \cos(\theta)R}{2\mu}$), which is common among flows dominates by capillarity. From Eq. 7 we can also see that a critical contact angle exists for capillary imbibition ($\theta < 90°$), meaning that imbibition will only occur if the liquid-solid interface already prefers the wetted case [8]. It has been shown that flow through tubes with non-circular cross sections follow this law, with variations to the diffusivity based on geometric properties [27]. Flow through open microchannels also follows a diffusive process [28]. It has been shown that hemiwicking also obeys the diffusive process [6], [7], [8], [9]. Bico et al. found that there also exists a critical angle for hemiwicking to occur [5], see in Eq. 8.

$$\cos(\theta_C) = \frac{1 - \phi_S}{r - \phi_S} \tag{8}$$

Here ϕ_S denotes the solid fraction of surface that remains dry during hemiwicking (for example the tops of cylindrical pillars), and r is the surface roughness. As $r > 1$ and $\phi_S \leq 1$, Eq. 9 will always give a critical angle $0 \leq \theta_C < 90$. This again shows an intermediate between surface wetting and porous wicking [8]. Using Eq. 6 as a basis, many studies have been completed deriving a theoretical hemiwicking diffusivity for a variety of pillar spacing and sizing parameters based on a balancing of the driving and resistive drag forces, some of which are detailed below.

Driving and Resisting Forces

The general method for modeling a hemiwicking array is by balancing a driving force, often made up of capillary forces and Laplace pressures, with a resisting drag force. As described in the "Stokes Flow" section, it is extremely hard to accurately analyze the drag of arbitrary shapes at low Reynold's numbers. A circular cross sectional area is one of the most studied geometries in this regime, and combined with the fact that cylindrical microstructures are relatively easy to fabricate compared to structures with sharp edge, leads to the fact that most studied have been performed on cylindrical microstructures of varying spacing parameters. Studies by Bico et al., Ishino et al., Kim et al., and Krishnan et al. are presented below. Method's for accounting for varying geometries are discussed, as well as limitations of each method. For all cases, spacing and sizing parameters are expressed based on the convention of Krishnan et al., given in Figure 3. S_y is the distance from one pillar to the next pillar in the same row, in the direction perpendicular to flow. S_x is the distance between consecutive rows, in the direction of flow. α is the skew of the array, and h and d are the height and diameter of the pillars, respectively.

12
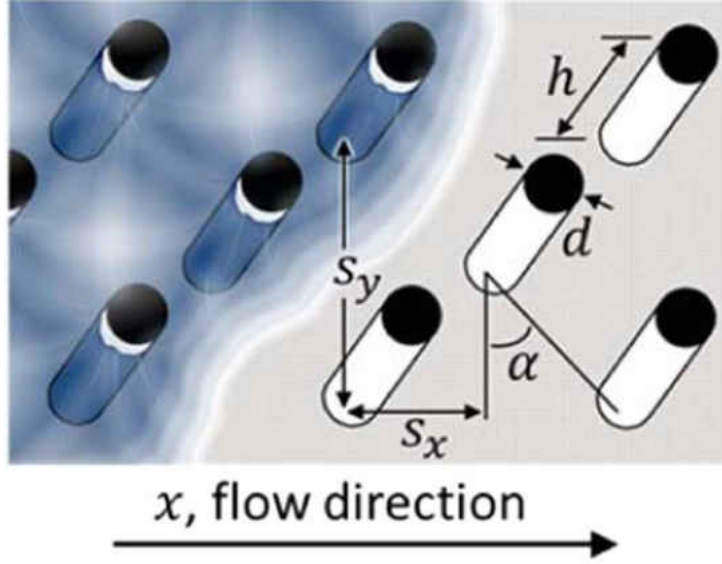
Figure 3: Spacing parameters of systematically microstructured surfaces, taken from Krishnan et al [6].

Bico et al. studied square arrays ($\alpha = 0$) of cylindrical micropillars. The forcing function was derived by the expression $dE = -\Delta P_L dV$. Here dE and dV are incremental changes in the surface energy and liquid volume, respectively, as the fluid climbs the array. dV is a function of ϕ_S and the roughness element height (h). The drag was estimated via the Poiseuille flow model. The balancing of these two forces gave the diffusion law [5]:

$$L^2 = \frac{2[\cos(\theta) - \cos(\theta_c)]\gamma h}{3\beta \cos(\theta_c) \mu} t \tag{9}$$

Here β is a scaling factor that arises from the application of Poiseuille flow to the pillars themselves, and θ_c is taken from Eq. 8. This model is useful in that it takes into account the surface energy of the solid (via the contact angle θ). The main limitation in this case is that β is a function of pillar spacing and sizing parameters, and was not derived analytically [5].

13

Ishino et al. also performed experiments on square arrays, with the constraint that $S_x = S_y = 10 \ \mu m$, and with a constant d value of 1 µm. Their derivation split into two regimes that were determined by the dominate form of drag: pillar sides and the bottom solid surface. The driving force was a simple surface energy minimization that gave $F_D = \gamma(r - 1)$. Kim et al. later showed that this model is only valid in the case of $\theta = 0$ [7].

For pillar heights shorter than the pillar spacing, the dominate form of drag arises from the bottom surface and gives F_{R1}. For pillar heights larger than the pillar spacing, the dominate form of drag arises from the sides of the pillars and gives F_{R2}. Taking Stokes flow assumptions for the velocity field, resisting forces for the two regimes were found to be:

$$F_{R1} \sim \frac{\mu \dot{L} L}{h} \quad , \quad F_{R2} \sim \frac{\mu \dot{L} h L}{S_x^2 \ln \frac{2S_x}{d}} \tag{10}$$

where L is the length into the array the fluid has propagated and $\dot{L}$ is its time derivative (velocity). Performing the proper force balance gives two distinct regimes of diffusivity [9]:

$$D_1 = \frac{2\pi \gamma h^2 d}{3\mu S_x^2} \quad , \quad D_2 = \frac{\gamma d}{2\mu} \left(\ln \left(\frac{2S_x}{d} \right) - 1.31 \right) \tag{11}$$

As stated, the sizing and spacing parameter restrictions limit the use of this equation. In addition to this, the equation does not take into account the surface energy of the solid, and (as Kim observed) assumes a microscopic contact angle of zero.

Kim et al. expanded the modeling of hemiwicking surfaces by accounting for possible array skewness ($\alpha \neq 0$). They again assumed a contact angle of zero in order to produce the forcing function $F_D = \gamma(1 - r)$. In order to generate a velocity field, they took the no slip condition at the

base and sides of pillars and the shear-free condition along the top. Two regions were identified with separate flow profiles: (I) the region between rows where the fluid is not in contact with any pillars, and (II) the region in which the flow was in contact with the pillars (see Figure 4).
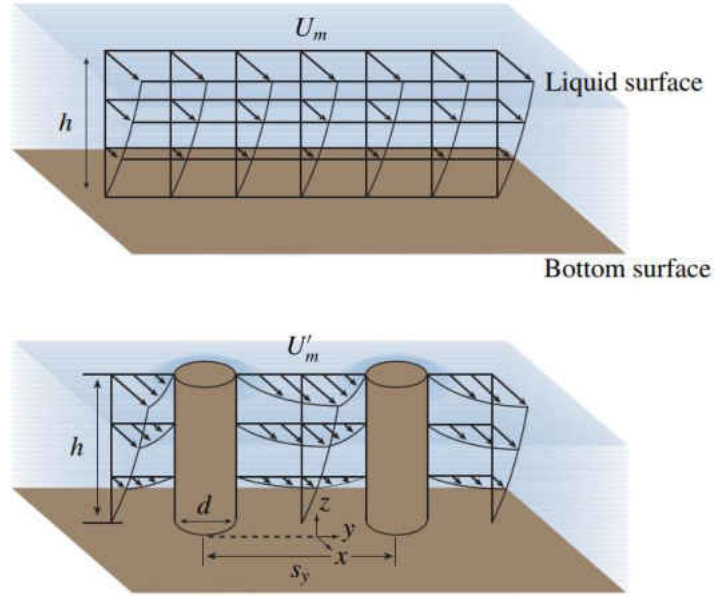
Figure 4: Flow velocity regions – region (I) is the top image while region (II) is the bottom image. Taken from Kim et al. [7].

Kim et al. calculated the total resistive force due to the sum of shear forces acting on the bottom surface in region (I) and both the bottom surface and pillar sides in region (II). This resulted in a resisting force, and diffusivity value [7]:

$$F_R = \mu \dot{L} L \left(\frac{1}{h} + \frac{r-1}{S_y - d} \right)$$ (12)

$$D = \frac{\gamma}{\mu} \frac{(r-1)}{1 + \frac{h(r-1)}{S_y - d}}$$ (13)

15

This equation is extremely useful as it does not separate based on regimes of dominate drag form, as Ishino's does. As stated earlier, it can also successfully be used for non-square spacing parameters. However, it again does not take into account surface energy variations, assuming a contact angle of zero degrees.

Kim et al. also investigated the microscopic case of meniscus extension from a single pillar and found two regimes for the forcing function: one dominated by the surface energy minimization as the fluid climbs the pillar, and the other dominated by the Laplace pressure due to the meniscus curvature. They found the microscopic extension x to scale as $t^{\frac{1}{3}}$ for the first case and t in the second case [7].

Krishnan et al. attempted to correlate experimental meniscus extensions (x_o) to a Laplace pressure driving force through arrays with varying skewness. This gave the driving force as:

$$F_D = \frac{\gamma h^2}{x_o^2} \tag{14}$$

They neglected viscous drag from the bottom surface, instead experimentally finding a drag coefficient via traditional methods:

$$F_R = \frac{1}{2} \rho \dot{L}^2 C_d \frac{hd}{S_y S_x} \tag{15}$$

Here, ρ is the fluid density, and C_d is of the form $C_d = \frac{C}{Re_d}$ [6]. This eliminates the density from Eq. 14 and makes the drag a function of velocity, which is common practice in the Stokes flow regime. The authors float the concept of a limiting Reynold's number based on the meniscus extension and initial spreading velocity of a droplet on a flat substrate ($Re_{x_0,v_0} = \frac{x_o v_o \rho}{\mu}$). They

16

argue that the solid-liquid interfacial dynamics of a hemiwicking surface can be characterized by this value, just as the solid-liquid interfacial properties of a smooth surface are captured by the equilibrium contact angle θ. Combining the resisting and driving forces and accounting for the limiting case, Krishnan et al. gives their diffusivity law as:

$$L^2 = \frac{2\gamma h s_x (s_y - 1)(f - 1)^{\frac{1}{2}}}{95\mu x_o^2} \qquad (16)$$

where the scalar value 95 represents the best fit for the constant C. This model is useful in that the surface energy variation is theoretically incorporated into x_o [6]. However, this meniscus extension is experimentally found, and no derivation for it analytically is presented, which presents a challenge when attempting to design structures based on the model.

Anisotropic Wetting

Anisotropic wetting surfaces is an emerging focus with direct applications in micro-scale cooling technologies. The ability to focus flows on local hot-spots would have vast implications in next-generation heat sink design, as well as other microfluidic applications [31]. Anisotropic droplet wetting has been observed for surfaces micropatterned with grooves, as well as asymmetric microstructure shapes. These anisotropies can exist either perpendicular (x vs y) or parallel to each other (-x vs x) [10], [11], [12]. Asymmetric roughening introduces local energy barriers that cannot be accounted for by either traditional surface roughening models (Wenzel model) or theoretical hemiwicking models that only incorporate the macroscopic surface energy change into the driving function [10]. Unidirectional wetting in microchannels with asymmetric microstructures has been shown to be caused by asymmetric curvature formation and consequent uneven Laplace pressures within the fluid [13].

Fully unidirectional wetting is an exaggerated form of anisotropic wetting. Yang et al. produced unidirectional wetting through slanted micropillar arrays and investigated the anisotropic contact angles that resulted [10]. Triangular micropillars have been shown to form uneven menisci via stability differences as a fluid climbs the flat side vs pointed side of the micropillar [14]. In the cases of both the triangular and slanted micropillars, the degree of asymmetry of the structures themselves as well as the spacing parameters of the structures influenced the local energy barriers, and these parameters could be varied to produce either anisotropic or unidirectional wetting [10], [14].
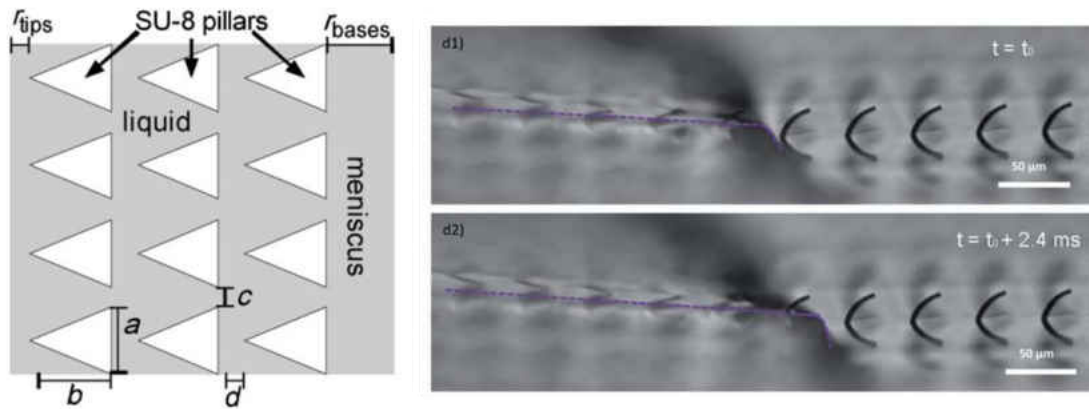

Figure 5: Examples of asymmetric microstructures that caused anisotropic wicking. Triangular micropillars fabricated by Jokenin et al. are pictured on the left while slanted microstructures fabricated by Yang et al. are pictured on the right [14], [10].

Hemiwicking Applications

The development of superhydrophilic hemiwicking surfaces has vast applications in thermal engineering. Enhanced wetting characteristics have been found to vastly increase the critical heat flux in pool boiling experiments, beyond results expected from traditional surface roughening models [3]. Rahman et al. found that increased "wickability" was, in fact, "the single

key factor in dictating critical heat flux on structured superhydrophilic surfaces with negligible contact angles" [3].

Superhydrophilic microstructures introduce an enhanced, steady film curvature over flat surfaces. It has been shown that enhanced film curvature can strongly influence heat and mass transfer characteristics in thin-film evaporation [32]. In addition to this, hemiwicking structures can provide a stable thin-film meniscus region, which accounts for over 50% of the total heat transfer during film evaporation [4], [33]. The intrinsic meniscus, thin-film meniscus, and absorbed layer are seen in Figure 5. Superhydrophilicity can also increase condensation rates, and has been a natural method for moisture harvesting in many animals that survive in arid climates [32], [34]. Superhydrophilic surfaces are also of interest for anti-fogging properties as well as photocatalytic self-cleaning surfaces [35].
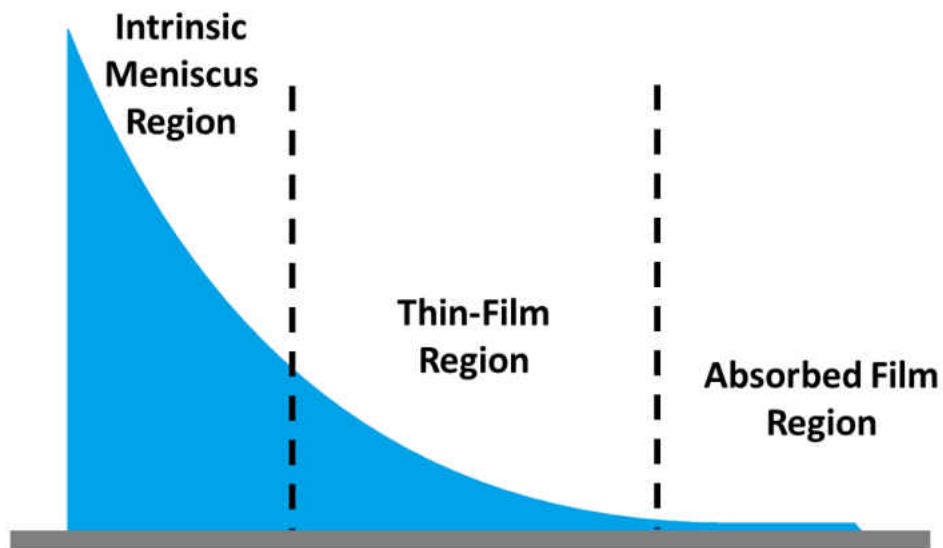
*Figure 6: The defined meniscus regions.*

CHAPTER 3: EXPERIMENTAL SETUP AND PROCEEDURE

Overview

Samples were produced at Oak Ridge National Laboratory's Center for Nanophase Material Science. Macroscopic propagation trials were completed over the entire array in order to quantify the anisotropic quality of the arrays. Microscopic high-speed interferometry trials were conducted in order to analyze the meniscus curvature evolution of the thin-film meniscus region as the fluid propagates between individual pillars. Microscopic side-angle trails were conducted at the last few rows of the arrays in both directions in order to analyze both the intrinsic meniscus curvature and the meniscus stability against the flat and curved faces of the pillars. All experiments were conducted in standard laboratory settings.

Sample Fabrication

Samples were fabricated at Oak Ridge National Laboratory's Center for Nanophase Material Sciences' Nanofabrication Laboratory utilizing a Nanoscribe Pro GT laser lithography system capable of two-photon polymerization. The substrates were silicon (Si) wafers with a thickness of approximately 0.50 mm. A thin-film of Al_2O_3, of thickness ~100 nm was deposited over the sample after nanofabrication in order to produce a constant surface energy value utilizing an Oxford Atomic Layer Deposition system. A lack of deposition would cause chemical heterogeneity on the surface, further complicating the interfacial dynamics of the system. All samples were observed via scanning electron microscopy utilizing both the Phenom XL and Zeiss Merlin FE measurement devices in order to ensure mechanical integrity of the pillars. Figure 7 shows results of this SEM imaging for selected samples.
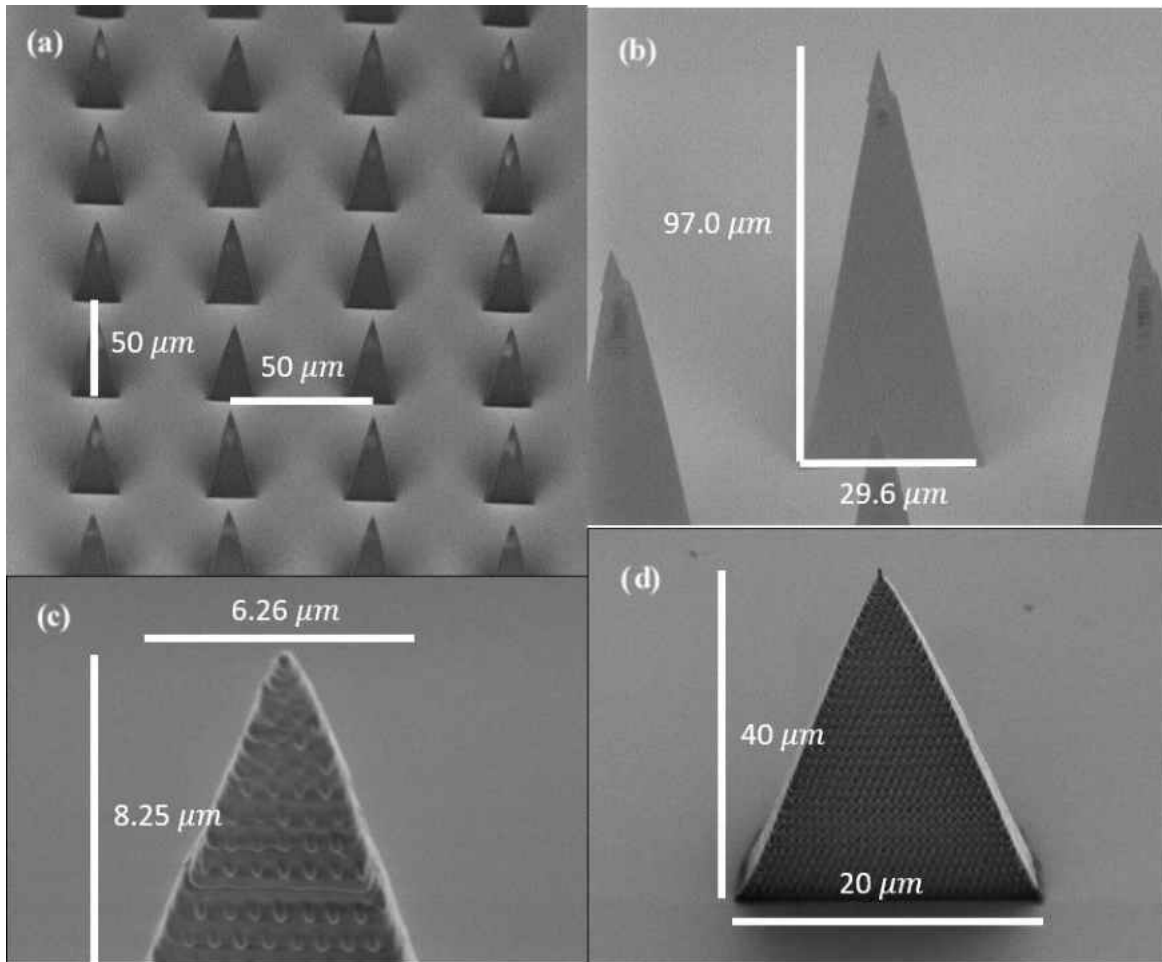
Figure 7: SEM images of micropillar structures captured at ORNL Center for Nanophase Material Sciences Nanofabrication Lab's Merlin Phenom SEMs. (a) sample H array (b) sample G single pillar (c) the tip of a sample G pillar with a resolution of 200 nm (d) sample A single pillar.

<u>Sample Parameters</u>

The sizing and spacing parameters are shown in Figure 8. Pillars were half-conical in nature (see Figures 6 and 7). Flow approaching the flat face of the pillars was labelled kiddie wicking, as it exhibited lower flow rates than that of flow approaching the curved face, which was labelled diamond wicking.
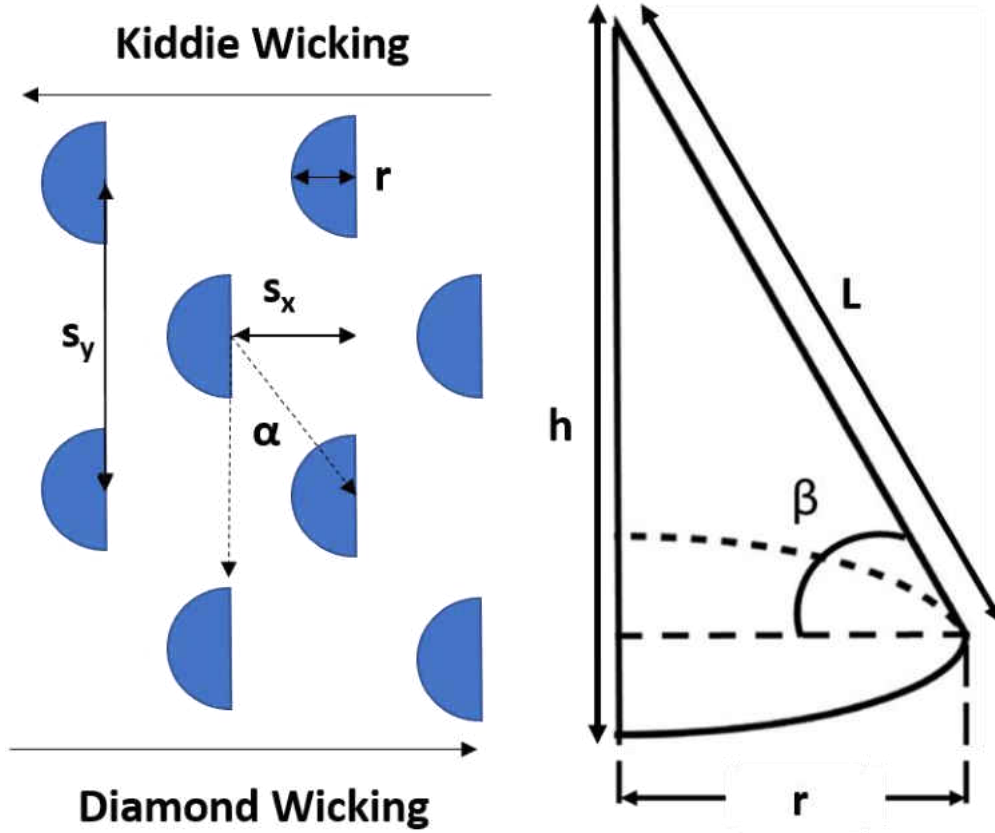
Figure 8: Sizing and spacing parameters utilizing during the experiment. These are the same spacing conventions used by both Krishnan et al. and Kim et al.

Arrays were 4 mm x 2 mm. Array skew values (α) of 0° and 45° were used. Pillar heights (h) ranged from 45 μm to approximately 105 μm. Pillar radius's (r) varied from 10 μm to 15 μm. The half-cone angle β is used as a measure of the asymmetricity of the pillars themselves: $\beta = \arctan(\frac{h}{r})$. Our pillar half-cone angle angles then range from 70° to 83°. L is defined as the shortest length from the base radius to the top of the half cone, given by $L^2 = r^2 + h^2$. A roughness factor, which defines the proportion of total area to projected area of the microstructure array, is given for half-conical pillars in Eq. 17.

$$f = 1 + \frac{hr + \frac{\pi r L_s}{2} - \frac{\pi r^2}{2}}{s_y s_x} \qquad (17)$$

Roughness factors range from 1.36 to 2.49 for the fabricated samples. A full table of sample parameters is given in Table 1 below.

Table 1: Sample parameters

	S_x (μm)	S_y (μm)	r (μm)	α (°)	h (μm)	h_m (μm)	f
A	40	80	10	45	50	41	1.36
B	40	80	10	45	70	59	1.52
C	40	80	10	45	90	71	1.68
D	40	80	15	45	60	57	1.63
E	40	80	15	45	75	68	1.80
F	40	80	15	45	90	76	1.98
G	40	80	15	45	105	97	2.16
H	50	50	10	0	50	44	1.46
I	50	50	10	0	70	58	1.66
J	50	50	10	0	90	76	1.87
K	50	50	15	0	60	58	1.80
L	50	50	15	0	75	67	2.03
M	50	50	15	0	90	86	2.26
N	50	50	15	0	105	102	2.49
O	40	80	15	45	45	39	1.45
P	50	50	15	0	45	44	1.58

Full-Array Wicking Tests

In order to verify the diffusive and anisotropic nature of the wetting motion, a vertical full array wicking experiment was completed. The sample was suspended firmly above a reservoir of liquid (liquids used in this study include ethanol and isopropanol) and a high-speed camera was focused on the entire sample. The reservoir was brought up to the sample until the bottom of the microstructure array was submerged, at which point hemiwicking would occur. The hemiwicking

motion was captured by the high-speed camera and analyzed to find the experimental diffusivity of each sample in the Diamond and Kiddie directions. On average, three trials were completed in both the Diamond and Kiddie directions for each sample. The setups for the full-array wicking tests and side-angle wicking tests were similar, with the only difference being the orientation of the surface normal with respect to the camera, and the objective utilized. Figure 9 below shows the setup utilized for those experiments.
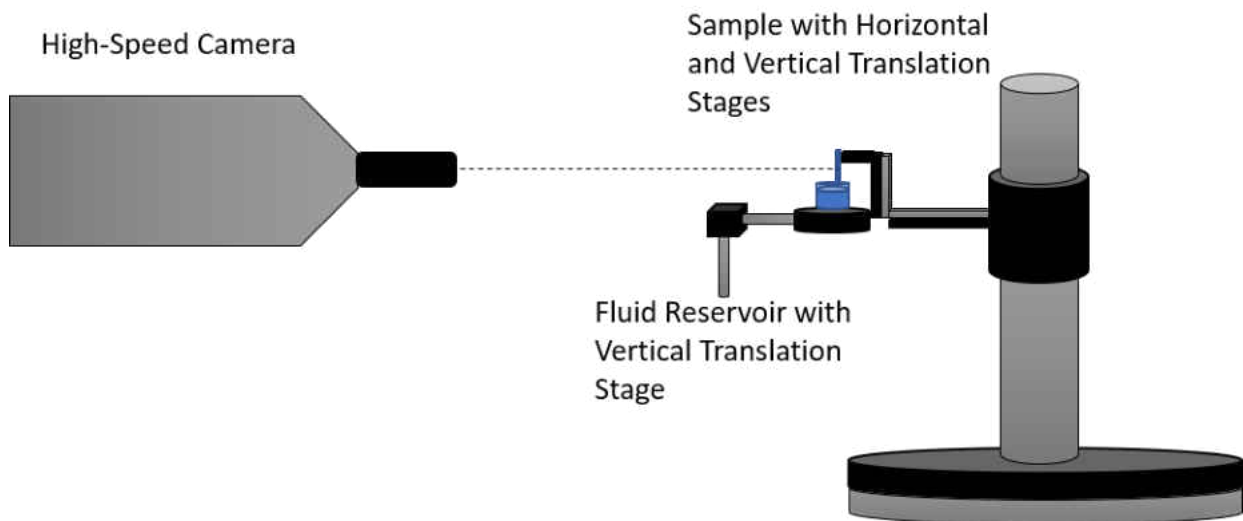
Figure 9: Experimental setup for full array wicking and side-angle tests.

High-Speed Interferometry Tests

The system utilized by Arends et al. is modified in order to perform high-speed interferometry experiments [36]. Monochromatic light (in the form of a blue laser) is used to create an interference fringe pattern on a high-speed camera, which is then analyzed within ImageJ and Matlab. Figure 10 demonstrates the experimental setup of the interferometry trials.
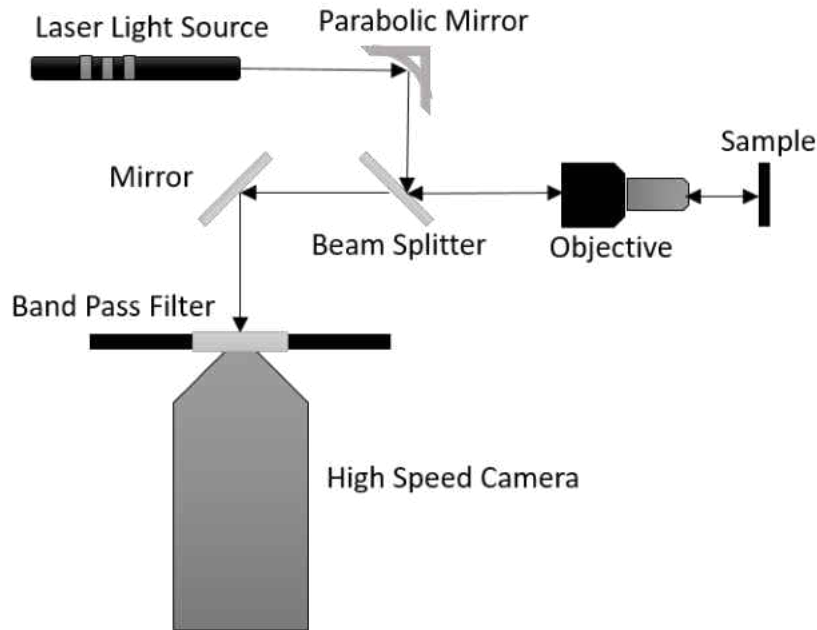
Figure 10: Experimental setup for interferometry trials, tracking the single wavelength light path through the optical setup.

Monochromatic light (WDLasers rated 450 nm and 2000 mW, tested at 454 nm) is powered by a GW INSTEK PSP-2010 variable power supply to control brightness of image. This light is reflected off a parabolic mirror (with UV Enhanced Al coating, reflective focal length of 15 mm, parental focal length of 7.5 mm) to further focus the light, then reflected off a 50-50 UV fused silica (UVFS) beam splitter into an objective (50X Mitutoyo Plan Apo NIR Infinity Corrected Objective) and focused on the sample. Reflected light passes back through the beam-splitter and reflects off a silver mirror and through a band pass filter (450 nm ± 10 nm) in order to subtract stray white light, and into a Phantom v12.1 high speed camera, operating at 2000 frames/second. Figure 11 shows the resulting thin film fringe patterns.

Camera resolution defined a lower limit to fringe spatial distance, so analysis was limited to the thin-film meniscus region, from the apparent contact line to approximately 1 µm in height.
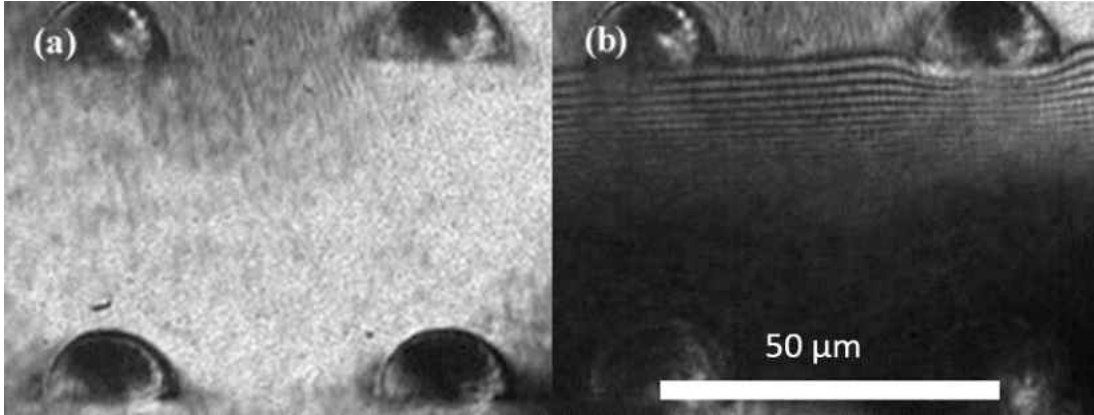
Figure 11: Example of interferometry raw data for sample H (a) background image with no fluid present (b) fringe patterns during wicking.

<u>Side-Angle Wicking Tests</u>

Utilizing the same setup as the macroscopic propagation tests, side angle videos captured the intrinsic meniscus evolution at the end of pillar arrays. A frame rate of 2000 frames/second was utilized for this experiment. The end was used as the slowest wicking occurs at the largest length into the array. This allowed more frames to be captured at the same frame rate.

Side angle videos were first corrected utilizing available ImageJ software [37]. As a slight angle with respect to the camera normal was inevitable, image scales in the x and y direction were directly yielded from known quantities in the images, namely the flow direction spacing (S_x) and the pillar heights (h). Once scaled, images were rotated so the surface plane was in the horizontal, and flow took place from left to right. Videos were then analyzed frame-by-frame utilizing in-house LabVIEW software. The in-house LabVIEW software provided x and z coordinates for the meniscus extension contact line (x_r, y_r) and pillar contact point (x_l, z_l), as well as contact angles at both locations (θ_r, θ_l). Videos captured both the intrinsic meniscus extension between pillars and the meniscus rise up the pillars after contact had been made with the next row. Samples were prone to foreign objects depositing on the surface during initial full-array vertical wicking tests

26

(for example, dust in the air). These foreign particles inhibited hemiwicking motion, causing zippering to occur early in some samples and others to cease wicking completely. Previous studies show that the fluid's effect on hemiwicking motion is fully captured via two parameters: viscosity and surface tension. Therefore, a single fluid is sufficient for providing information in inter pillar wetting dynamics, and this data can be scaled to predict the same motion for other fluids. Figure 12 shows original images captured during side-angle wicking experiments, as well as the scaled and rotated image used during LabVIEW analysis.
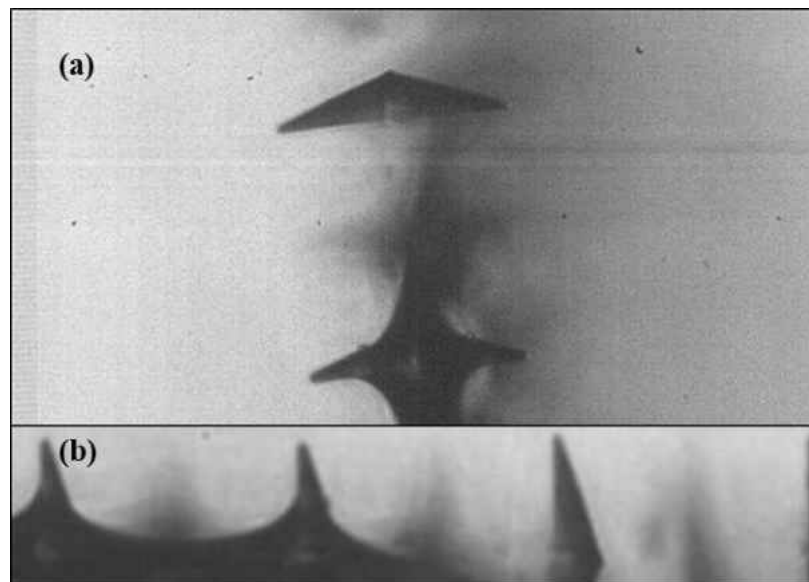
Figure 12: A frame taken from side-angle wicking trials of Sample O (a) original image and (b) image scaled and rotated within ImageJ in preparation for LabVIEW analysis.

CHAPTER 4: RESULTS AND DISCUSSIONS

<u>Full-Array Diffusivity Results</u>

The anisotropic and diffusive nature of the samples was captured via macroscopic wicking tests. Figure 13 displays the diffusive nature of the hemiwicking motion for select samples, while Figure 14 shows the diffusivity of each sample in the Diamond and Kiddie directions.
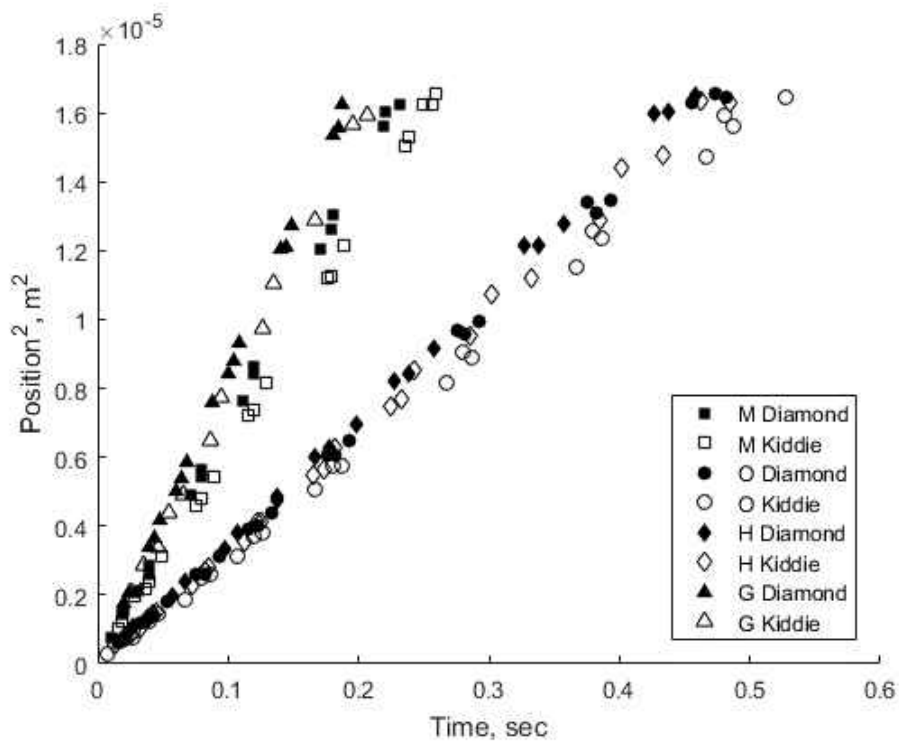
Figure 13: The diffusive nature of samples H, M, O, and G with ethanol.
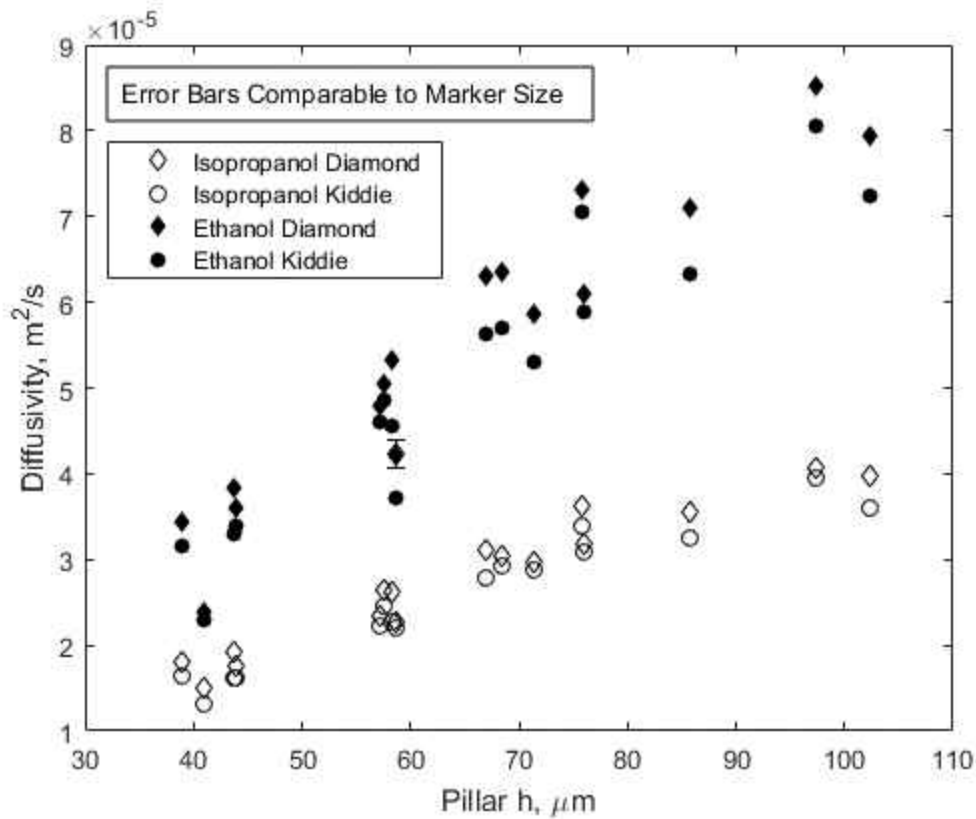
Figure 14: Diffusivities of all samples in the Diamond and Kiddie directions.

There is a strong trend of increasing diffusivity with an increase in the pillar height, which is to be expected as increasing pillar height increases the roughness (f) of the array. It is also noted that Diamond wicking occurs at a faster rate than Kiddie wicking for all trials, however, the exact value of this increase and a trend with pillar height is not discernable. Standard error bar sizes for diffusivity values are approximately the same size as marker points, and only the largest error is shown in the figure. All diffusivity and standard error values are displayed in Table 2 (below).

Table 2: Diffusivity and standard error values for full-array wicking tests

	Ethanol				Isopropanol			
	$D_{Diamond}$ (mm²/s)	D_{kiddie} (mm²/s)	$\sigma^{x}_{Diamond}$ (mm²/s)	σ^{x}_{Kiddie} (mm²/s)	$D_{Diamond}$ (mm²/s)	D_{kiddie} (mm²/s)	$\sigma^{x}_{Diamond}$ (mm²/s)	σ^{x}_{Kiddie} (mm²/s)
A	23.78	23.05	0.45	0.89	14.95	13.11	0.26	0.25
B	42.19	37.06	1.62	0.78	22.74	22.01	0.29	0.31
C	58.52	52.97	0.85	0.82	29.67	28.82	0.45	0.32
D	47.86	46.05	0.64	0.82	23.40	22.25	0.20	0.27
E	63.50	56.96	0.36	0.73	30.47	29.17	0.30	0.28
F	73.10	70.59	1.11	0.94	36.29	33.86	0.45	0.17
G	85.27	80.44	0.27	0.85	40.63	39.48	0.32	0.31
H	35.92	34.01	0.36	0.39	17.51	16.21	0.09	0.11
I	50.45	48.71	0.68	0.68	26.48	24.61	0.19	0.31
J	60.89	58.84	0.46	0.69	31.89	30.86	0.27	0.25
K	53.22	45.67	0.49	0.64	26.17	22.69	0.22	0.16
L	62.98	56.22	0.25	1.06	31.14	27.80	0.18	0.20
M	70.91	63.38	0.57	0.39	35.46	32.50	0.29	0.32
N	79.50	72.42	0.60	0.62	39.66	36.00	0.23	0.22
O	34.42	31.57	0.27	0.53	18.03	16.43	0.09	0.11
P	38.35	32.89	0.52	0.30	19.15	16.14	0.18	0.10

Here standard error (σ^{x}) is calculated based on Eq. 18:

$$\sigma^{x} = \frac{\sigma}{\sqrt{n}}$$

(18)

where σ is taken as the standard deviation of L^2/t values, and n is the total number of points extrapolated from videos.

<u>High-Speed Interferometry Results</u>

After fringe patterns are recorded using high-speed videography, the height of the thin-film meniscus at each fringe location is found utilizing Eq. 19, assuming an initial height of zero at the contact line.

$$z_j = z_{j-1} + (x_j - x_{j-1}) \tan \left(\frac{\lambda}{2n_f(x_j - x_{j-1})} \right) \tag{19}$$

Here λ is the wavelength of the light, n_f is the index of refraction of the fluid, x_j is the j'th element of the fringe position array, with the first element being at the contact line and the last element being the last discernable fringe, and z_j is the meniscus height at x_j. In line with the work of Wang et al., a second order polynomial is fitted to this data [Wang]:

$$z = ax^2 + bx + c \tag{20}$$

Experimental data based on Eq. 18, along with corresponding polynomial fits,
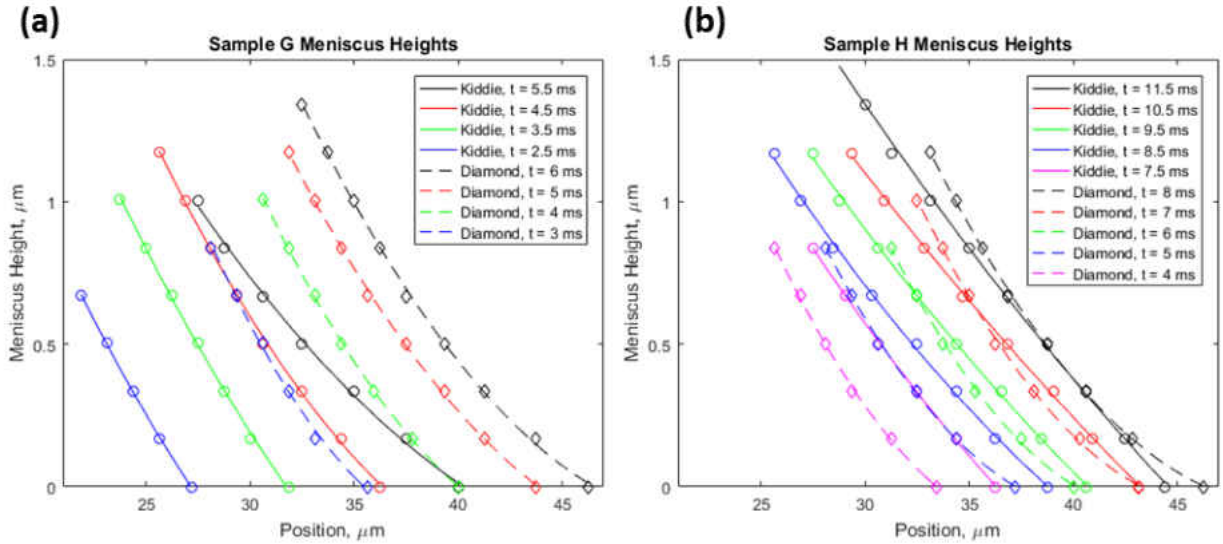
Figure 15: (a) meniscus height vs position for Sample G and (b) meniscus height vs position for Sample H.

Intrinsic meniscus angles and curvatures can then be extrapolated from this fit using Eq. 21 and 22.

$$\theta(x) = -\frac{180}{\pi} \arctan \left(\frac{dz}{dx} \right) = -\frac{180}{\pi} \arctan(2ax + b) \tag{21}$$

$$\kappa(x) = \frac{\left|\frac{d^2z}{dx^2}\right|}{\left(1 + \left(\frac{dz}{dx}\right)^2\right)^{\frac{3}{2}}} = \frac{2a}{(4a^2x^2 + 4abx + b^2 + 1)^{\frac{3}{2}}} \tag{22}$$

The absolute value operator is neglected as all second derivatives are positive. Results for Sample H and Sample G with ethanol, based on Eq. 22 are presented below.
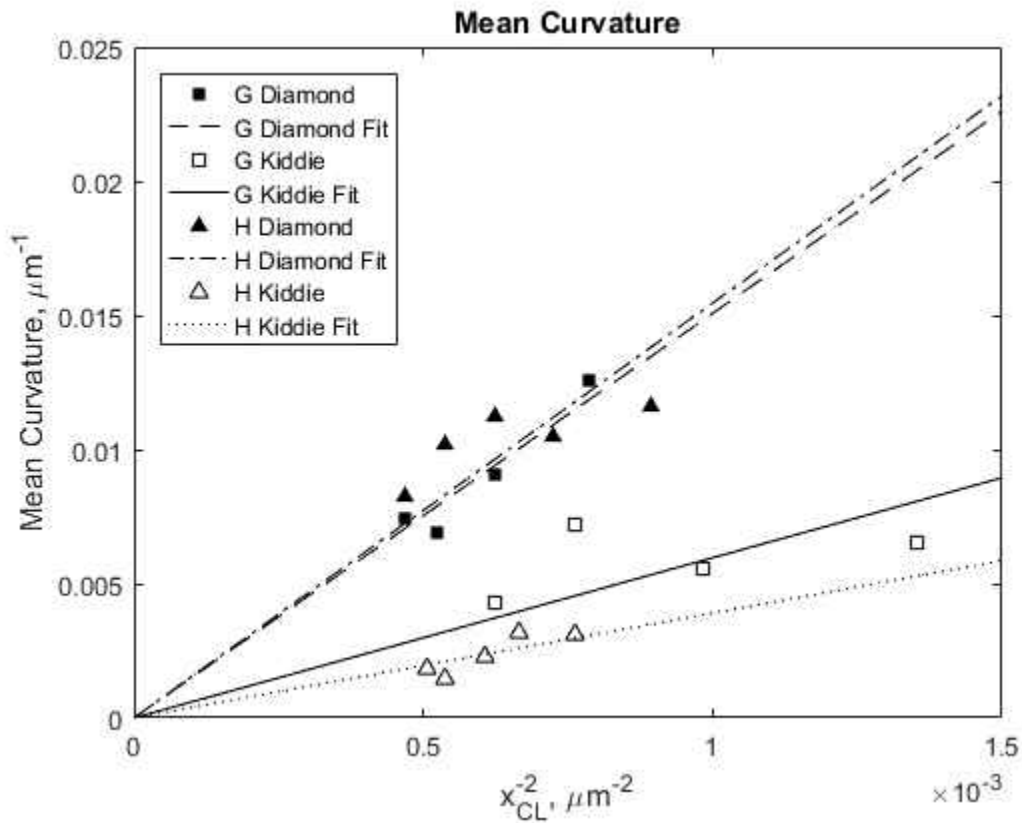
Figure 16: Mean curvature plotted against standard curvature scaling, for interferometry trials.

There is a clear trend, marked by the lines of best fit through the origin – mean curvature values found through interferometry data properly scale with traditional scaling techniques for curvature, validating the use of this method for curvature analysis. There is a significant difference in the slope between Diamond wicking and Kiddie wicking, indicating greater overall curvature

in the meniscus during Diamond wicking. Of interesting note is that Sample G and Sample H have almost identical curvature values for Diamond wicking although the sizing parameters of the two arrays are vastly different, and Sample G has an overall diffusivity 2.3 times greater than that of Sample H. This discrepancy is most likely due to the skewed nature of the Sample G array, which has shown to decrease drag compared to square arrays for samples with similar pillar densities [7].

<u>Side-Angle Extensions Results</u>

Figure 17 gives microscopic side-angle meniscus propagation results for Sample H in both the Diamond and Kiddie directions.
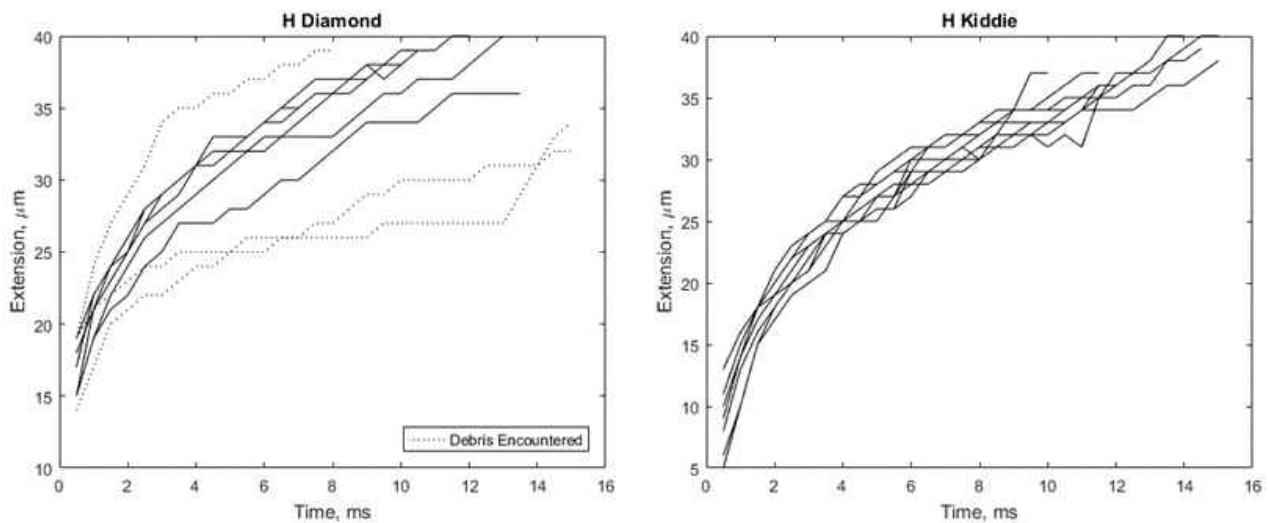
Figure 17: Side-angle results (a) meniscus extension from pillar vs time for Sample H Diamond and (b) meniscus extension from pillar vs time for Sample H Kiddie.

From side angle videos, it is noted that the fluid quickly rises up the sides of the pillars in both the Diamond and Kiddie cases in approximately the first 2 ms. After this initial sudden rise, the fluid either halts its rise or propagates upwards at an extremely reduced rate. Figure 17 shows that this initial propagation results in a quicker meniscus extension propagation in early time scales

33

for Diamond wicking compared to Kiddie wicking. This is most likely due to increased meniscus instability against a curved surface in the case of Kiddie wicking. A similar occurrence was noted by Jokenin et al. utilizing triangular micropillars. The same stability difference is expected to be observed in half-conical micropillars, but this instability should be less pronounced due to the curved nature of the pillar rather than the sharp corner utilized by Jokenin et al. [14].

The average curvature of the meniscus can be calculated using contact point coordinates and contact angles using the first part of Eq. 22. The average first and second derivative of the meniscus can be found using Eq. 23 and Eq. 24:

$$\frac{d^2z}{dx^2}_{avg} = \frac{\tan(\theta_r) - \tan(\theta_l)}{\Delta x} \tag{23}$$

$$\frac{dz}{dx}_{avg} = \frac{z_r - z_l}{\Delta x} \tag{23}$$

Here Δx is the horizontal distance between the pillar and surface contact points. For Diamond wicking this is equal to the meniscus extension value, but for Kiddie wicking, the slope of the curved pillar surface must be taken into account. θ_l, θ_r, z_l, and z_r are the angle with respect to the horizontal and contact point height of the pillar contact point and surface contact point, respectively. LabVIEW software captured contact angles with respect to the horizontal, and not the pillar surface, so no adjustments were necessary to resolve contact angles. Figure 18 shows the mean curvature results, again plotted against x_{CL}^{-2}.
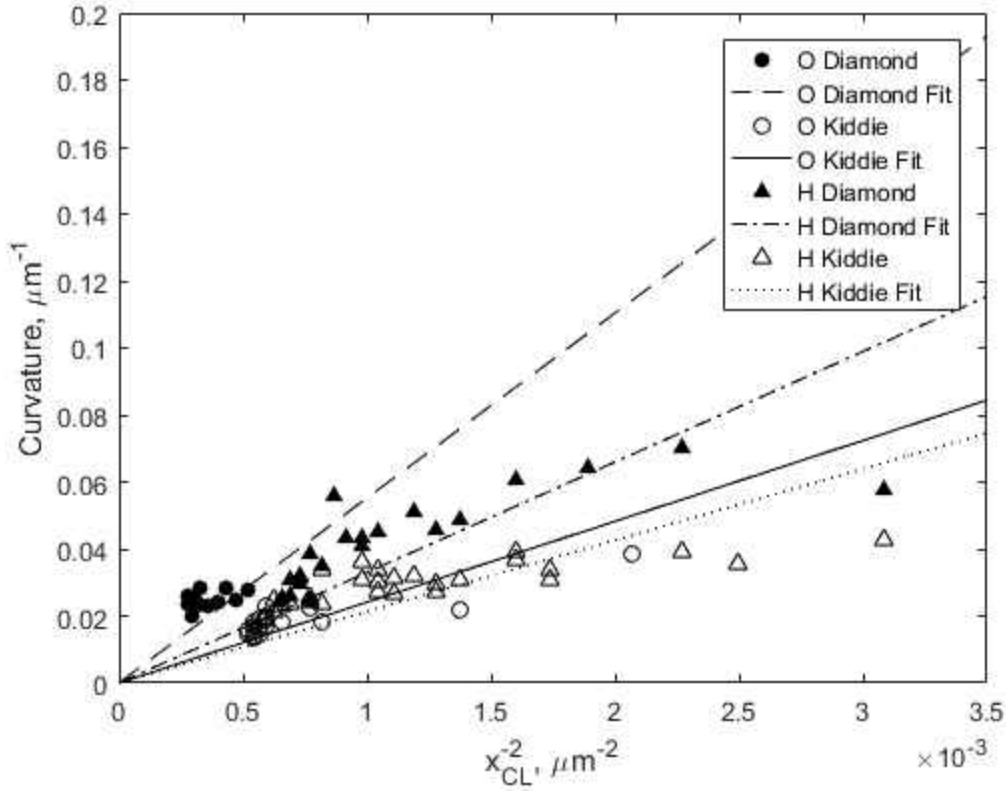
Figure 18: Mean curvature plotted against standard curvature scaling for side angle trials. Code for fits were taken from [39].

Increased meniscus curvatures are observed during side angle wicking for Diamond direction over Kiddie direction, in agreement with interferometry results (Figure 16). It is noted that at early time scales (high x_{CL}^{-2} values), curvature values are smaller than predicted by traditional scaling laws. This is due to larger contact angles at the beginning of inter-pillar propagation compared to later time scales, seen in Figure 19. As has been noted, early time scale propagation is dominated by surface energy minimization due to fluid climbing up the pillar, so this discrepancy is still in line with theory.
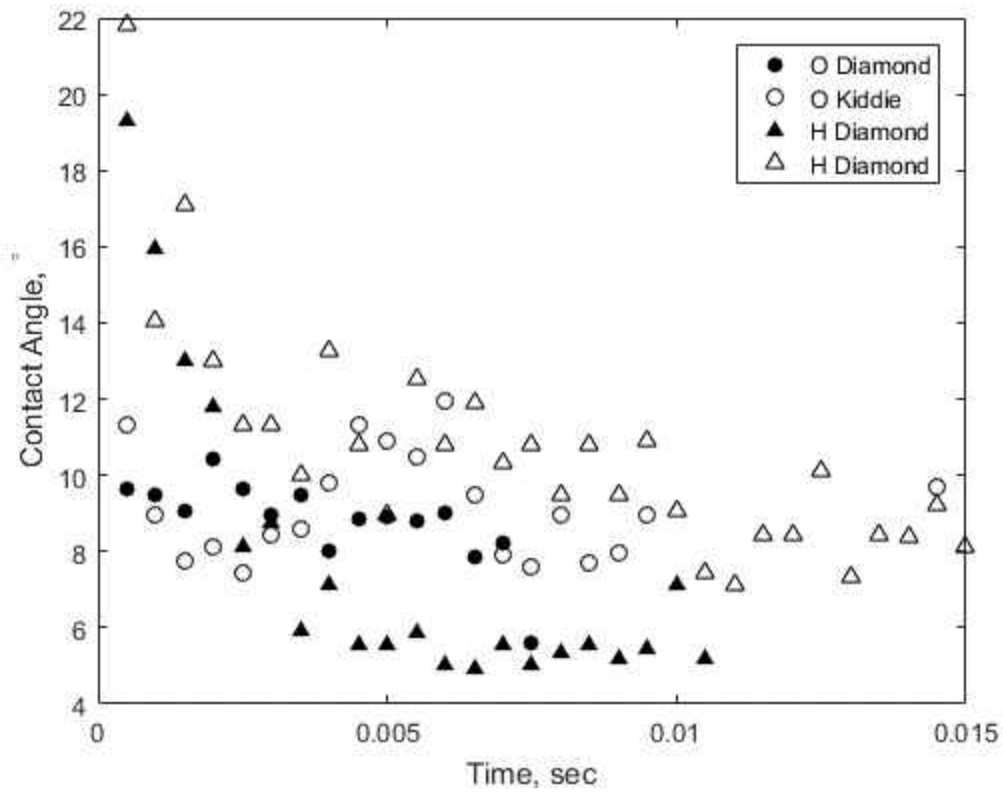
Figure 19: Surface contact angles for side-angle trials

Contact angles are significantly larger at the beginning of inter-pillar propagation than at later time scales for Sample H. The same trend is present, but not as pronounced for Sample O. this is in agreement with Figure 18, where curvature values at early time scales are significantly less than theory for Sample H, but are more in line with theory for Sample O.
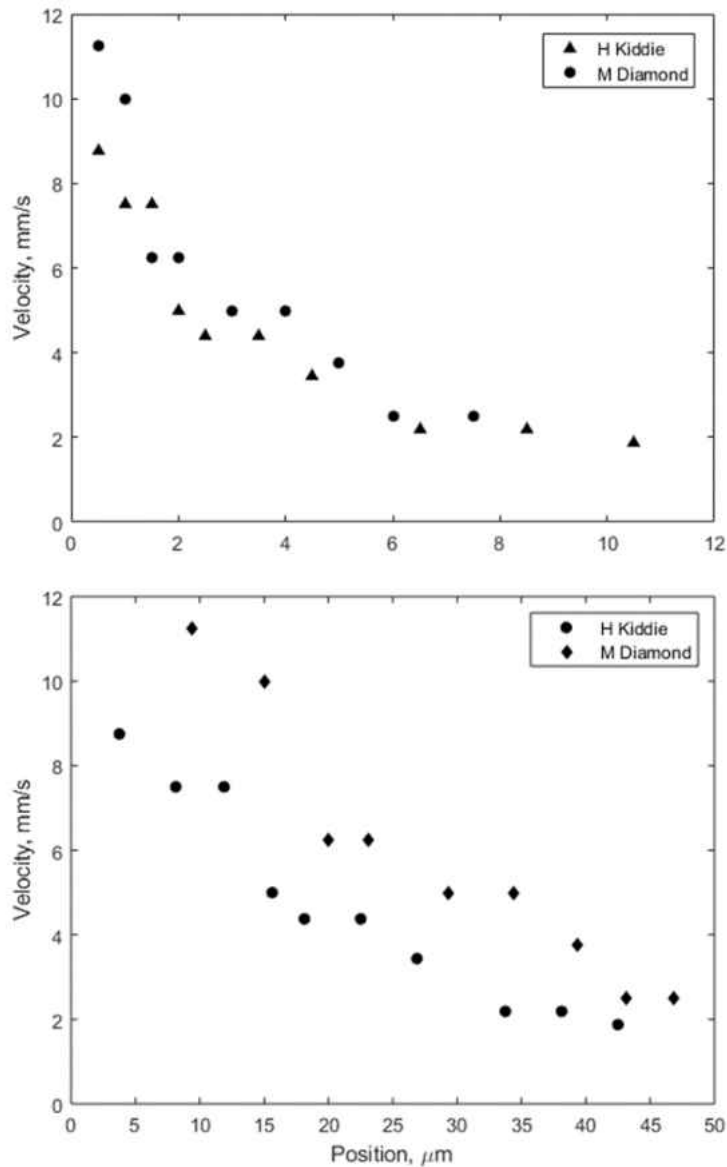
Figure 20: Velocity vs time and position for the fastest side-angle trial and the slowest side angle trial

Inter-pillar propagation for the Diamond wicking of the fastest sample microscopically analyzed and the Kiddie wicking of the slowest sample microscopically analyzed is shown in Figure 20. It is observed that M Diamond has significantly larger velocities over the entire inter-pillar distance than H Kiddie.
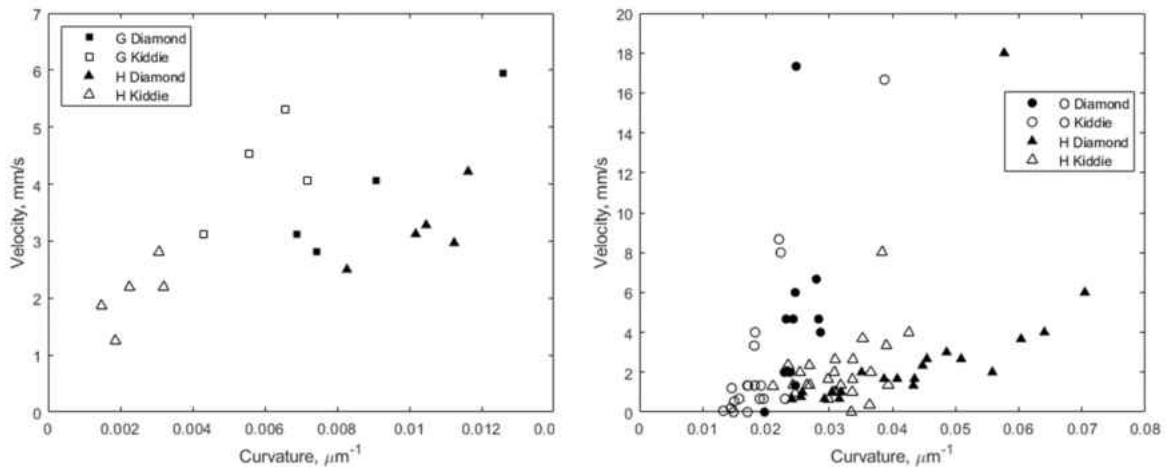
Figure 21: Velocity vs curvature for (left) film-film meniscus propagation and (right) intrinsic meniscus propagation

Figure 21 shows interferometry (left) and side-angle videography (right) meniscus propagation velocity vs curvature. Since thin film measurements were only possible with low contact angles (due to fringe spatial resolution) far from the pillar, the trend of increased velocities with curvature is evident. The trend is not as evident in intrinsic calculations, as curvature is not the driving force at early time scales during inter-pillar propagation. This accounts for the high velocity outlier points. Lower spatial resolution of side-angle results meant that, at low contact angles (far from the pillar, see Figure 19), when the thin film propagation beyond the intrinsic meniscus is high, the velocity of the true contact point is not observed. This accounts for low velocity measurements in intrinsic meniscus propagation. Overall, higher curvature is observed to correlate to higher velocity measurements when curvature is the significant driving force.

A Short Note on Drag

A comprehensive review of drag on non-uniform objects in the Stoke's flow regime and derivation of a drag model for half-conical pillars is beyond the scope of the current study.

However, intuition and a basic understanding of fluid mechanics would suggest that the drag coefficient around the half-conical pillars in the diamond direction would be less than or equal to the drag coefficient in the kiddie direction for the same Reynold's number range. This would imply that the anisotropic nature of the half-conical pillars is either entirely dependent on the forcing functions described above, or a combination of the forcing functions and the drag function. In either scenario, diamond wicking is predicted to occur at a faster rate than kiddie wicking.

Conclusion

Anisotropic hemiwicking designs show great promise for increased cooling efficiencies by utilizing complex flow patterns to conform to local hot spot densities in thin-film evaporation, as well as pool, flow, and thin-film boiling. In this study, asymmetric half-conical microstructure arrays were fabricated via two-photon polymerization, and anisotropic and diffusive qualities were characterized by visual videography. High-speed interferometry and side-angle videography are utilized to study the evolution of the thin-film and intrinsic meniscus curvature, respectively, during inter-pillar front propagation. It is verified by both side-angle and interferometry data that an increase in propagation front velocity during Diamond wicking is accompanied by an increased meniscus curvature over Kiddie wicking. Curvature values found through side angle and interferometry trials are in general agreement with each other. It is theorized that this increase in curvature leads to larger Laplace pressures that drive the motion of hemiwicking at later stages of inter-pillar propagation. Curvature is found to scale well with traditional methods within the same trial, further validating the experiments. These results are exciting for future optimization of the anisotropic nature of asymmetrically microstructured surfaces.

CHAPTER 5: FUTURE WORK AND MODIFICATIONS

The present work detailed above is among the first steps towards optimization of anisotropic micropillars. Understanding the exact nature and cause of the curvature differences can lead towards a more complete model of asymmetric hemiwicking. Further optimization of anisotropic quality would include exact predictive models on meniscus instability and curvature evolution for a variety of asymmetric shapes, as it has been found that both of these phenomena effect the anisotropic forcing function. An exact relation between meniscus curvature and asymmetric quality of the microstructures is also needed.

Computational fluid dynamics simulations detailing the nature of drag around asymmetric structures in the Stokes flow regime are necessary to fully realize the above model, as drag differences may be significant and affect the application of these models.

Finally, laboratory studies on the microscopic effects of anisotropic hemiwicking surfaces in thin-film evaporation and boiling processes will allow for the implementation of these surfaces into industrial applications. Understanding the complete effect of anisotropic wetting on local hot spots will allow for the realization of complex flow patterns meant to deal with non-uniform surface heat fluxes.

REFERENCES

[1] T. M. Germain, T. A. Chowdhury, J. Carter, S. A. Putnam, "Measuring heat transfer coefficients for microchannel jet impingement using time-domain thermoreflectance", *2018 17th IEEE Intersociety Conference on Thermal and Thermomechanical Phenomena in Electronic Systems (ITherm)*, San Diego, CA, 2018, pp. 449-454. Accessed on Mar. 1, 2020. [Online]. Available: https://ieeexplore.ieee.org/stamp/stamp.jsp?tp=&arnumber=8419486.

[2] A. M. Briones, J. S. Ervin, S. A. Putnam, L. W. Byrd, and L. Gschwender, "Micrometer-sized water droplet impingement dynamics and evaporation on a flat dry surface" *Langmuir*, vol. 26 , iss. 16, pp. 13272-13286, July 2010. Accessed on Mar. 1, 2020. [Online]. Available: https://doi.org/10.1021/la101557p.

[3] M. M. Rahman, E. Olceroglu, M. McCarthy, "Role of wickability on the critical heat flux of structured superhydrophilic surfaces", *Langmuir*, vol. 30, iss. 37, pp 11225-11234, Aug. 2014. Accessed on Mar. 1, 2020. [Online]. Available: https://doi.org/10.1021/la5030923.

[4] R. Ranjan, J. Y. Murthy, S. V. Garimella, "Analysis of the wicking and thin-film evaporation characteristics of microstructures", *Journal of Heat Transfer,* vol. 131, iss. 10, pp. 101001-101012, Oct. 2009. Accessed on Mar. 1, 2020. [Online]. Available: https://doi.org/10.1115/1.3160538.

[5] J. Bico, C. Tordeux, D. Quere, "Rough wetting", *EPL (Europhysics Lett.),* vol. 55, no. 2, 2001. Accessed Mar. 1, 2020. [Online]. Available: https://iopscience.iop.org/article/10.1209/epl/i2001-00402-x/pdf.

[6] S. R. Krishnan, J. Bal, S. A. Putnam, "A simple analytic model for predicting the wicking velocity in micropillar arrays' *Scientific Reports*, vol 9, no. 20074, Dec. 2019. Accessed on Mar. 1, 2020. [Online]. Available: https://doi.org/10.1038/s41598-019-56361-7.

[7] J. Kim, M. Moon, H. Kim, "Dynamics of hemiwicking" *Journal of Fluid Mechanics*, vol. 800, pp. 57-71, June 2016. Accessed on Mar. 1, 2020. [Online]. Available: https://doi.org/10.1017/jfm.2016.386.

[8] J. Bico, U. Thiele, D. Quere, "Wetting of textured surfaces", *Colloids and Surfaces A: Physiochemical and Engineering Aspects*, vol. 206, iss. 1-3, pp. 41-46, July 2002. Accessed Mar. 9, 2020. [Online]. Available: https://doi.org/10.1016/S0927-7757(02)00061-4

[9] C. Ishino, M. Reyssat, E. Reyssat, K. Okumura, D. Quere, "Wicking within forests of micropillars", *EPL (Europhysics Lett.),* vol. 79, no. 5, Aug. 2007. Accessed Mar. 11, 2020. [Online]. Available: DOI: 10.1209/0295-5075/79/56005

[10] X. M. Yang, Z.W. Zhong, E.Q. Li, Z.H. Wang, W. Xu, S.T. Thoroddsen, X.X. Zhang, "Asymmetric liquid wetting and spreading on surfaces with slanted micro-pillar arrays", *Soft Matter*, vol. 9, iss. 46, pp. 11113-11119, Oct. 2013. Accessed on Mar. 9, 2020. [Online]. Available: DOI: 10.1039/C3SM51809D.

[11] D. Xia, L.M. Johnson, and G. P. Lopez, "Anisotropic wetting surfaces with one-dimensional and directional structures: fabrication approaches, wetting properties and potential applications", *Advanced Materials*, vol. 24, iss. 10, pp. 1287-1302, Feb. 2012. Accessed on Mar. 1, 2020. [Online]. Available: https://doi.org/10.1002/adma.201104618.

[12] K.J. Kubiak and T.G. Mathia, ""Anisotropic wetting of hydrophobic and hydrophilic surfaces – modelling by lattice boltzmann method". *Procedia Engineering*, vol. 79, pp. 45-48, 2014. Accessed Mar. 1, 2020. [Online]. Available: https://doi.org/10.1016/j.proeng.2014.06.307.

[13] J. Feng, J. Rothstein, "One-way wicking in open micro-channels controlled by channel topography", *Journal of Colloid and Interface Science*, vol. 404, pp. 169-178, 2013. Accessed Mar. 9, 2020. [Online]. Available: DOI:10.1016/jcis.2013.02.052.

[14] V. Jokinen, M. Leinikka, and S. Franssila, "Microstructured surfaces for directional wetting" *Advanced Materials*, vol. 21, iss. 47, pp. 4835-4838, Dec. 2009. Accessed on Mar 1, 2020. [Online]. Available: https://doi.org/10.1002/adma.200901171.

[15] A. T. Chwang and T. Y. Wu, "Hydromechanics of low-Reynolds-number flow. Part 1. Rotation of axisymmetric prolate bodies", *Journal of Fluid Mechanics*, vol. 63, iss. 3, April 1974. Accessed on Mar. 1, 2020. [Online]. Available: https://doi.org/10.1017/S0022112074001819.

[16] S. Kim, S. J. Karrila, H. Brenner, *Microhydrodynamics. Principles and Selected Applications*. Stoneham, MA: Butterworth – Heinemann Publishing, 1991.

[17] C. Priest, R. Sedev, J. Ralston, "Asymmetric Wetting Hysteresis on Chemical Defects", *Physical Review Letters*, vol. 99, iss. 2, July 2007. Accessed on Mar. 9, 2020. [Online]. Available: https://doi.org/10.1103/PhysRevLett.99.026103.

[18] M. E. Schrader, "Young-Dupre revisited", *Langmuir*, vol. 11, iss. 9, pp. 3585-3580, Sep. 1995. Accessed Mar. 9, 2020. [Online]. Available: https://doi.org/10.1021/la00009a049

[19] L. Courbin, J. C. Bird, M. Reyssat, and H. A. Stone, "Dynamics of wetting: from inertial spreading to viscous imbibition", *Journal of Physics: Condensed Matter*, vol. 21, num. 46, Oct. 2009. Accessed on Mar 9, 2020. [Online]. Available: https://iopscience.iop.org/article/10.1088/0953-8984/21/46/464127/pdf.

[20] N. K. Adam, H. K. Livingston, "Contact angles and work of adhesion", *Nature*, vol. 182, iss. 128, July 1958. Accessed Mar. 10, 2020. [Online]. Available: https://doi.org/10.1038/182128a0

[21] A. B. D. Cassie, "Contact angles", *Discussions of the Faraday Society*, vol. 3, 1948. Accessed Mar. 10, 2020. [Online]. Available: https://doi.org/10.1039/DF9480300011

[22] L. J. Douglas Frink, A. G. Salinger, "Wetting of a chemically heterogeneous surface", *Journal of Chemical Physics*, vol. 110, no. 12, pp. 5969-5977, Mar. 1999. Accessed Mar. 9, 2020. [Online]. Available: https://doi.org/10.1063/1.478497.

[23] R. N. Wenzel, "Resistance of solid surfaces to wetting by water", Ind. Eng. Chem, vo. 28, no. 8, Aug. 1936. Accessed Mar. 10, 2020. [Online]. Available: https://doi.org/10.1021/ie50320a024

[24] J.G. Fan, X.J. Tang, and Y.P. Zhao, "Water contact angles of vertically aligned Si nanorod arrays", *Nanotechnology*, vol. 15, no. 5, pp. 501-504, Aug. 2003. Accessed Mar. 9, 2020. [Online]. Available: DOI:10.1088/0957-4484/15/5/017.

[25] M. Nosonovsky, "On the range of applicability of the wenzel and cassie equations", *Langmuir*, vol. 23, no. 19, pp. 9919-9920, Aug. 2007. Accessed Mar. 9, 2020. [Online]. Available: https://doi.org/10.1021/la701324m

[26] L. Gao, T.J. McCarthy, "How Wenzel and Cassie Were Wrong", *Langmuir,* vol. 23, no. 7, pp. 3762-3765. Feb. 2007. Accessed Mar. 9, 2020. [Online]. Available: https://doi.org/10.1021/la062634a.

[27] J. Kim, H. Y. Kim, "On the dynamics of capillary imbibition", *Journal of Mechanical Science and Technology*, vol. 26, pp. 3795-3801, 2012. Accessed Mar. 9, 2020. [Online]. Available: https://doi.org/10.1007/s12206-012-1006-2.

[28] D. Yang, M. Krasowska, C. Priest, M.N. Popescu, J. Ralston, "Dynamics of capillary-driven flow in open microchannels", *Journal of Physical Chemistry C*, vol. 115, iss. 38, pp. 18761-18769, 2011. Accessed Mar. 9, 2020. [Online]. Available: https://doi.org/10.1021/jp2065826.

[29] G. K. Batchelor, *An Introduction to Fluid Dynamics*, Cambridge, UK: Cambridge University Press, 1967. Accessed Mar. 11, 2020. [Online]. Available: https://doi.org/10.1017/CBO9780511800955

[30] E. W. Washburn, "The Dynamics of Capillary Flow", Physical Review, vol. 17, iss. 3, Mar. 1, 1921. Accessed Mar. 13, 2020. [Online]. Available: https://doi.org/10.1103/PhysRev.17.273

[31] O. Bliznyuk, H. P. Jansen, E. S. Kooij, H. J. W. Zandvliet, B. Poelsema, "Smart Design of Stripe-Patterened Gradient Surfaces to Control Droplet Motion", Langmuir, vol. 27, iss. 17, pp. 11238-11245, July 25, 2011. Accessed Mar. 13, 2020. [Online]. Available: https://doi.org/10.1021/la201671w

[32] O. Wilhelmsen, T. T. Trinh, S. Kjelstrup, D. Bedeaux, "Influence of Curvature on the Transfer Coefficients for Evaporation and Condensation of Lennard-Jones Fluid from Square-Gradient Theory and Nonequilibrium Molecular Dynamics", *The Journal of Physical Chemistry A*, vol. 119, no. 15, pp 8160-8173, Mar. 18, 2015. Accessed Mar. 13, 2020. [Online]. Available: https://doi.org/10.1021/acs.jpcc.5b00615

[33] J. Owens, "Characteristics of Hydrogel-Wetted Thin Films", Master's Thesis, MAE, UCF, Orlando, Florida, May 24, 2017. Accessed Mar. 13, 2020. [Online]. Available: https://stars.library.ucf.edu/etd/5479

[34] A. Lee, M. Moon, H. Lim, W. Kim, and H. Kim, "Water harvest via dewing", *Langmuir*, vol. 28, pp. 10183-10191, June 2012. Accessed on Mar. 2, 2020. [Online]. Available: https://doi.org/10.1021/la3013987.

[35] K. Koch and W. Barthlott, "Superhydrophobic and superhydrophilic plant surfaces: an inspiration for biomimetic materials" *Philosophical Transactions of the Royal Society A*, vol. 367, iss. 1893, April 2009. Accessed on Mar. 2, 2020. [Online]. Available: https://doi.org/10.1098/rsta.2009.0022.

[36] A. A. Areds, T. M. Germain, J. F. Owens, and S. A. Putnam, "Simultaneous reflectometry and interferometry for measuring thin-film thickness and curvature". AIP Review of

Scientific Instruments, vol. 89, iss. 5, May 2018. Accessed on Feb. 26, 2020. [Online]. Available: https://doi.org/10.1063/1.5021704

[37] C. T. Rueden, J. Schindelin, M. C. Hiner, et al, "ImageJ2: ImageJ for the next generation of scientific image data" *BMC Bioinformatics* vol. 18, no. 529. 2017. Accessed on Mar. 1, 2020 [Online]. Available: doi:10.1186/s12859-017-1934-z

[38] R. Xiao, E. N. Wang, "Microscale Liquid Dynamics and the Effect on Macroscale Propagation in Pillar Arrays", Langmuir, vol. 27, iss. 17, pp. 10360-10364, July 2011. Accessed on Jan. 20, 2020. [Online]. Available: https://doi.org/10.1021/la202206p

[39] Mark Mikofski (2020). polyfitZero (https://www.mathworks.com/matlabcentral/fileexchange/35401-polyfitzero), MATLAB Central File Exchange. Retrieved March 19, 2020.